

# **Reverberation Mapping Analysis of the 2016 HST Campaign on NGC 4593**

Vorname Nachname

Universität XYZ

Betreuer: XYZ

September 8, 2025

## **Abstract**

Abstract

# Contents

<b>1</b>	<b>Introduction</b>	<b>4</b>
<b>2</b>	<b>Scientific Background</b>	<b>5</b>
2.1	Active Galactic Nuclei . . . . .	5
2.1.1	Structure and spectral Features of an AGN . . . . .	6
2.1.2	Classification . . . . .	8
2.1.3	Unification Model . . . . .	11
2.1.4	Variability . . . . .	12
2.2	Reverberation Mapping . . . . .	13
2.2.1	Principle . . . . .	13
2.2.2	Cross-Correlation Function and Lag Measurement . . . . .	14
2.2.3	Black-Hole Mass . . . . .	14
2.3	Bowen Fluorescence . . . . .	15
<b>3</b>	<b>Campaign and Analysis</b>	<b>17</b>
3.1	NGC4593 . . . . .	17
3.2	2016 Campaign by E. M. Cackett . . . . .	18
3.3	Intercalibration and Determination of AVG and RMS Spectra . . . . .	19
<b>4</b>	<b>Reverberation Mapping Analysis of NGC4593</b>	<b>21</b>
4.1	Line Determination . . . . .	21
4.2	Lightcurves . . . . .	23
4.2.1	Continua . . . . .	23
4.2.2	Emission Lines . . . . .	23
4.3	Line Profiles . . . . .	23
4.4	Time Lag and BH Masses . . . . .	23
4.5	Bowen Fluorescence . . . . .	23
<b>5</b>	<b>Discussion</b>	<b>29</b>

# List of Figures

2.1	Different components of an AGN. Adapted from (Mo, Bosch, and White 2010) Figure 14.3. . . . .	5
2.2	An example of Seyfert I and Seyfert II spectra illustrating their differences. Broad lines, such as the highlighted $H\alpha$ and $H\beta$ , are only present in the Seyfert I spectrum, whereas forbidden [O III] lines are visible in both cases. Adapted from (ResearchGate 2025). . . . .	9
2.3	Unification model of an AGN (Fermi Gamma-ray Space Telescope 2025). . . . .	12
3.1	A DSS image of NGC4593. . . . .	18
3.2	Comparison of the optical spectral range of the original spectra and the [O III] $\lambda 5007$ intercalibrated spectra from the 2016 campaign of NGC 4593. . . . .	20
3.3	Comparison of the optical spectral range of the avg and rms spectra from the original data and the [O III] $\lambda 5007$ intercalibrated data from the 2016 campaign of NGC 4593. . . . .	20
4.1	AVG RMS spectrum . . . . .	21
4.2	AVG RMS spectrum . . . . .	22
4.3	AVG RMS Spektrum . . . . .	24
4.4	AVG RMS Spektrum . . . . .	25
4.5	AVG RMS Spektrum . . . . .	26
4.6	AVG RMS Spektrum . . . . .	27
4.7	AVG RMS Spektrum . . . . .	28

# List of Tables

3.1 Overview of STIS Grating Characteristics (Space Telescope Science  
Institute 2025) . . . . . 18

# 1. Introduction

## 2. Scientific Background

### 2.1 Active Galactic Nuclei

Active Galactic Nuclei (AGN) refers to the central region of active Galaxies. Those objects are among the most luminous objects in the universe, with bolometric luminosities ranging from  $10^{41}$  to  $10^{48}$  erg s $^{-1}$ , outshining entire galaxies by several orders of magnitude (Bradley M. Peterson 1997). First explanation tries were unusually dense star clusters or repeated supernova explosions as power sources, but these models soon proved insufficient to account for the observed luminosities, which spans over the entire electromagnetic spectrum. Today it is understood, that these enormous luminosities are powered by accretion of matter onto a supermassive black hole (SMBH) in the center of the AGN. The most common model for this accretion is a hot, rotating accretion disk around the SMBH, which is responsible for most of the observed radiation (Shakura and Sunyaev 1973).

To provide a basic understanding of the structure and physical processes within AGN, the following sections will outline the key components, introduce the unification model that connects various AGN types, and summarize common classification schemes. A special focus will be on AGN variability, which plays a central role in the reverberation mapping analysis conducted in this thesis.

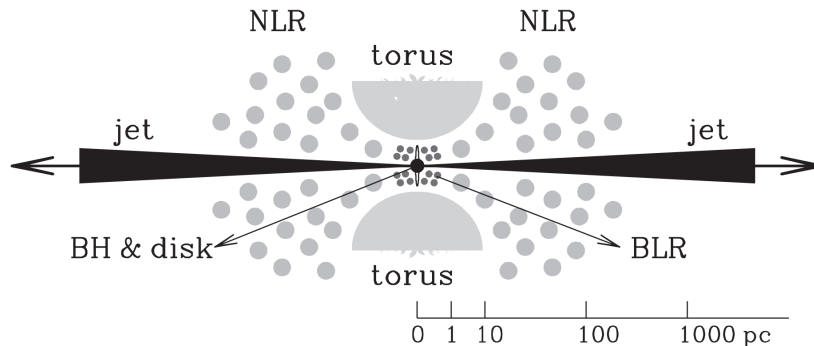


Figure 2.1: Different components of an AGN. Adapted from (Mo, Bosch, and White 2010) Figure 14.3.

### 2.1.1 Structure and spectral Features of an AGN

The structure of an AGN consists of several components, which are illustrated schematically in Figure 2.1. These include a central supermassive black hole (SMBH), an accretion disk that feeds the SMBH, a surrounding dusty torus, and ionized gas regions known as the broad-line region (BLR) and narrow-line region (NLR). In some AGNs, powerful relativistic jets are launched perpendicular to the accretion disk. However, these jets will not be discussed further in this section, as they are not relevant to the scope of this thesis.

#### Supermassive Black Hole and Accretion Disk

The center of an AGN is formed by a supermassive black hole (SMBH), with masses typically ranging from  $10^6 M_\odot$  to more than  $10^{10} M_\odot$ . While the SMBH itself does not emit radiation, it acts as the central engine for all observed AGN phenomena and dominates the gravitational potential in the innermost regions. Other than in inactive Galaxies, like the milky-way, the SMBH of an active galaxy is surrounded, by an accretion disk. But due to conservation of momentum, its matter doesn't just fall inside. It has to lose its angular momentum first, which happens due to the viscosity of the disks itself. Viscosity processes like turbulent friction or magnetorotational instability transports the angular momentum further out, which finally leads to the matter spiraling inward toward the SMBH, heating it up. The accretion disk itself is a geometrically thin and optically thick structure composed of ionized gas in differential rotation around the SMBH. The disk's composition is primarily ionized hydrogen and helium, with traces of heavier elements. It extends from the innermost stable circular orbit (ISCO) near the event horizon out to distances of several light-days. The radial extent of the disk is relatively small on galactic scales, typically ranging from a few light-hours to a few light-days, corresponding to about  $10^{-3}$  to  $10^{-2}$  pc (Netzer 2013; Hickox and Alexander 2018; Shakura and Sunyaev 1973).

Like mentioned the accretion process converts gravitational potential energy into heat, causing the disk to reach very high temperatures. As a result, a significant fraction of the gravitational energy of the matter is transformed into thermal radiation, which accounts for the enormous luminosity observed in AGNs and heats the accretion disk depending on the size of the SMBH. As an example, the maximum effective temperature for an accretion disk around a SMBH with  $M = 10^8 M_\odot$  is on the order of several  $\times 10^5$  K, leading to UV and optical emission. In comparison, disks around stellar-mass black holes reach much higher temperatures (up to



a few  $\times 10^6$  K), emitting mostly in X-rays. Due to the temperature gradient with hotter regions in the inner disk, the emitted spectrum can not be described as a single black-body. Instead, it results from combination of many black-body-like components at different temperatures, often referred to as a multi-color black-body. This creates a broad optical-UV continuum that cannot be fully described by simple black-body radiation. In addition, processes like electron scattering and relativistic effects near the black hole further modify the shape of the spectrum (Osterbrock 1989).

The ionizing photons, emitted by the continuum, play a crucial role for the other spectral features. They interact with the surrounding gas clouds near the nucleus, causing photo-ionization followed by recombination. This process leads to different types of strong emission lines, which are characteristic features of AGN spectra (Netzer 2013; Osterbrock 1989).

### **Broad-Line and Narrow-Line Region**

Geometrical above and below the accretion disk plain, lies a distribution of gas clouds, which are photo-ionized by the energetic photons of the accretion disk continuum. The innermost of these clouds is the broad-line region (BLR), located at distances of a few light-days to light-weeks from the central SMBH (see Figure 2.1). The BLR consists of dense gas clouds with electron densities of  $n_e \sim 10^9\text{--}10^{11}\text{cm}^{-3}$ , moving at high velocities of several thousand kilometers per second due to the strong gravitational influence of the SMBH. These velocities lead to a significant Doppler broadening of permitted emission lines and line widths of around  $3000\text{ km s}^{-1}$ . As described earlier, the BLR is primarily photo-ionized by the continuum radiation emitted from the accretion disk. As a result, the line emission from this region is strongly correlated with the continuum emission, which is particularly important for a reverberation mapping analysis, which will be discussed later in Section 2.2.

The exact geometry of the BLR remains uncertain, with models ranging from a spherical distribution of clouds to a flattened disk-like structure. Broad emission lines appear in permitted transitions such as  $\text{H}\alpha$ ,  $\text{H}\beta$  and  $\text{Ly}\alpha$ . (Netzer 2013; Osterbrock 1989; Bradley M. Peterson 1997)

Even further out lies the narrow-line region (NLR). The gas in this region moves at much lower velocities, resulting in emission lines with widths typically below  $1000\text{ km s}^{-1}$ . In contrast to the BLR, the NLR allows both permitted and forbidden transitions. Forbidden lines, such as  $[\text{O III}] \lambda 5007$ , arise because collisional de-excitation is inefficient at the relatively low densities of the NLR ( $n_e \sim 10^2\text{--}10^6\text{cm}^{-3}$ ) (Osterbrock 1989). The narrow  $[\text{O III}] \lambda 5007$  line was used to intercalibrate the

spectra of the various observations employed in this thesis (see Chapter 3).

## **Dusty Torus**

Surrounding the accretion disk and broad-line region is the dusty torus, a geometrically thick and optically dense structure composed of gas and dust. It extends from a radius, where dust can survive the intense radiation of the accretion disk, out to scales of a few parsecs. The torus likely has a clumpy distribution and plays a crucial role in the unified model of AGNs which will be discussed in a later section (Netzer 2013; Hickox and Alexander 2018). The dust in the torus absorbs a significant fraction of the UV and optical radiation emitted by the accretion disk and re-emits it thermally in the infrared. As a result, AGNs typically exhibit strong infrared emission, with the peak wavelength depending on the temperature of the dust in the torus. This reprocessed radiation provides an important observational signature and can be used to trace obscured AGN activity, especially in AGNs where the central region is hidden from direct view (Netzer 2013).

### **2.1.2 Classification**

As previously implied, AGN emit across the entire electromagnetic spectrum, with their emission characteristics strongly depending on their internal structure. Consequently, each AGN exhibits a unique spectral signature, based on which they have historically been classified.

These classifications are based on the differences in luminosity, emission-line profiles, and radio properties. Broadly, AGNs can be grouped into Seyfert galaxies, quasars, and radio galaxies. Seyfert galaxies are further subdivided based on the appearance of broad and narrow emission lines. Seyfert 1 galaxies exhibit both broad and narrow emission lines, where Seyfert 2 galaxies show only narrow emission lines. Besides those main classes there are additional subclasses including narrow-line Seyfert 1 galaxies (NLS1s), low-ionization nuclear emission-line regions (LINERs), and jet-dominated sources such as BL Lac objects or blazars (Antonucci 1993; C. Megan Urry and Padovani 1995).

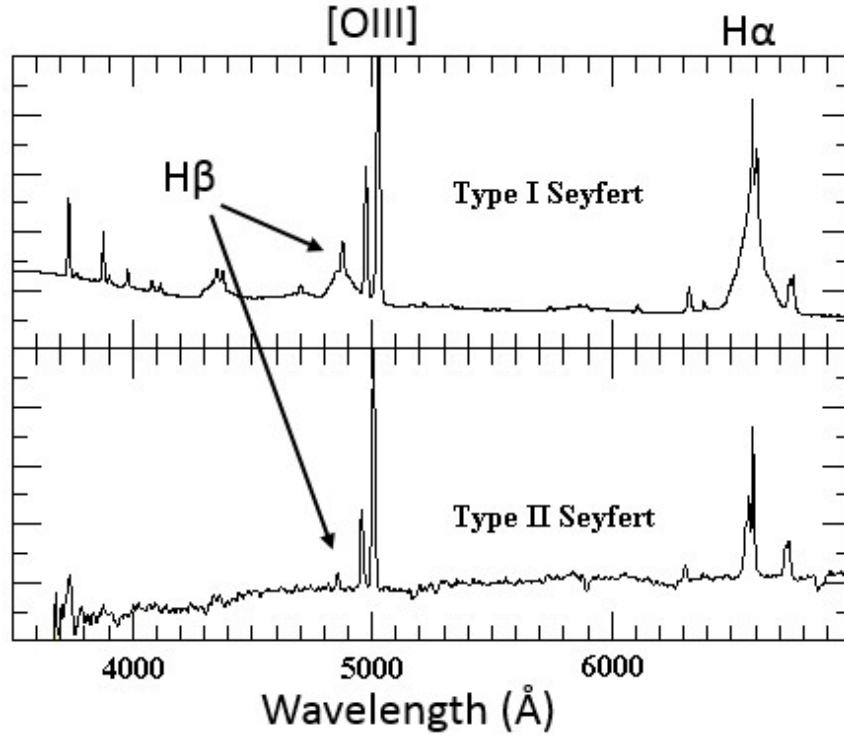


Figure 2.2: An example of Seyfert I and Seyfert II spectra illustrating their differences. Broad lines, such as the highlighted  $H\alpha$  and  $H\beta$ , are only present in the Seyfert I spectrum, whereas forbidden  $[O\ III]$  lines are visible in both cases. Adapted from (ResearchGate 2025).

### Seyfert Galaxies

Seyfert galaxies are named after Carl K. Seyfert, who in 1943 observed spiral galaxies characterized by exceptionally bright nuclei and prominent broad emission lines in their optical spectra (Seyfert 1943). For that they represent a class of AGN with bright nuclei and strong emission lines. Today, they are classified primarily based on the presence and width of permitted and forbidden low- and high-ionized emission lines. Figure 2.2 highlights the differences of the spectra of Type I and Type II Seyfert galaxies.

Seyfert 1 galaxies, of which NGC 4593 is an example, show both broad and narrow emission lines in their optical spectra. The broad lines, such as  $H\alpha$  and  $H\beta$ , have a full width at half maximum (FWHM) of typically several thousand kilometers per second and arise from the high-velocity BLR. In contrast, narrow lines, including prominent forbidden transitions like  $[O\ III]\ \lambda 5007$  or  $[N\ II]\ \lambda 6584$ , originate from the lower-velocity NLR (Osterbrock 1989; Bradley M. Peterson 1997). The presence of both components in the spectrum allows for a clear classification as a Seyfert 1 galaxy, which is the case for NGC4593. More to NGC4593 in section 3.1.

In comparison, Seyfert 2 galaxies lack these broad components in their optical spectra, likely due to orientation-dependent obscuration by the dusty torus. So the classification of a Seyfert galaxies strongly depends on the viewing angle of the observer, which is the key point for the Unified Model of AGN, which will be deepened in section 2.1.3.

Another notable subclass are the so-called narrow-line Seyfert 1 galaxies (NLS1s). Despite their classification as Seyfert 1, the broad permitted lines in their spectra exhibit unusually small widths, with  $\text{FWHM} < 2000 \text{ km s}^{-1}$ . They often show strong Fe II emission complexes and steep soft X-ray spectra. NLS1s are thought to have low-mass black holes accreting at high Eddington rates, suggesting they may represent a young evolutionary phase of AGN activity (Osterbrock and Pogge 1985; Netzer 2013).

## Others

Next to Seyfert galaxies, there are several other classes of AGN. Quasars, short for quasi-stellar radio sources, are even more luminous than Seyfert galaxies and are typically found at higher redshifts. While the host galaxies of Seyfert galaxies are still observable, quasars completely outshine their host galaxies. Since quasars show similar emission characteristics to Seyfert galaxies, the modern distinction is based mainly on luminosity: quasars are classified as high-luminosity AGNs, while Seyferts represent the lower-luminosity end (Netzer 2013).

Radio galaxies are defining another AGN class. They are characterized by their strong radio emission and prominent jets, often associated with elliptical host galaxies. When their jets are aligned close to our line of sight, they are observed as blazars or BL Lac objects, which exhibit rapid variability and featureless optical spectra due to relativistic beaming (Netzer 2013).

Finally, LINERs are low-luminosity AGNs with spectra dominated by low-ionization emission lines. The physical origin of their ionization mechanism is still debated, and in some cases, they may not be powered by accretion at all (Netzer 2013).

While these classifications are based primarily on spectral characteristics, many of the observed differences between AGN types can be attributed to orientation effects. The Unified Model of AGN provides a framework that explains this apparent diversity through a common internal structure, viewed from different angles.

### 2.1.3 Unification Model

The Unification Model of AGN, illustrated in Figure 2.3, proposes that the apparent diversity of AGN types arises primarily from differences in viewing angle and obscuration, rather than fundamentally different structures.

As shown in the figure, the observer's viewing angle relative to the AGN strongly determines the observed type. The dusty torus plays a key role here, as it surrounds the central region of the AGN—the accretion disk and the fast-moving BLR. If the observer's line of sight is blocked by the torus, only radio emission and narrow-line emission from the NLR outside the torus can be detected. In this case, the AGN appears as a Seyfert 2 galaxy, since the broad emission lines from the BLR and the optical/UV radiation from the accretion disk are obscured. The observer essentially views the AGN from a flat angle, looking directly at the torus.

If, on the other hand, the observer has a direct view into the central region of the AGN, not obscured by the torus, the fast moving gas clouds of the BLR as well as the optical/UV emission continuum from the accretion disk become visible. So both, broad and narrow emission lines, can be observed, which classifies it as a Seyfert 1 Galaxy. (C. Megan Urry and Padovani 1995)

Although the classical Unification Model treats AGN classification as fixed and purely geometry-driven, some AGNs have been observed to change their spectral type over time. These so-called "changing-look AGNs" challenge the purely orientation-based interpretation and suggest that intrinsic changes, such as variations in accretion rate or obscuring material, can also affect its classification (Ricci et al. 2022).

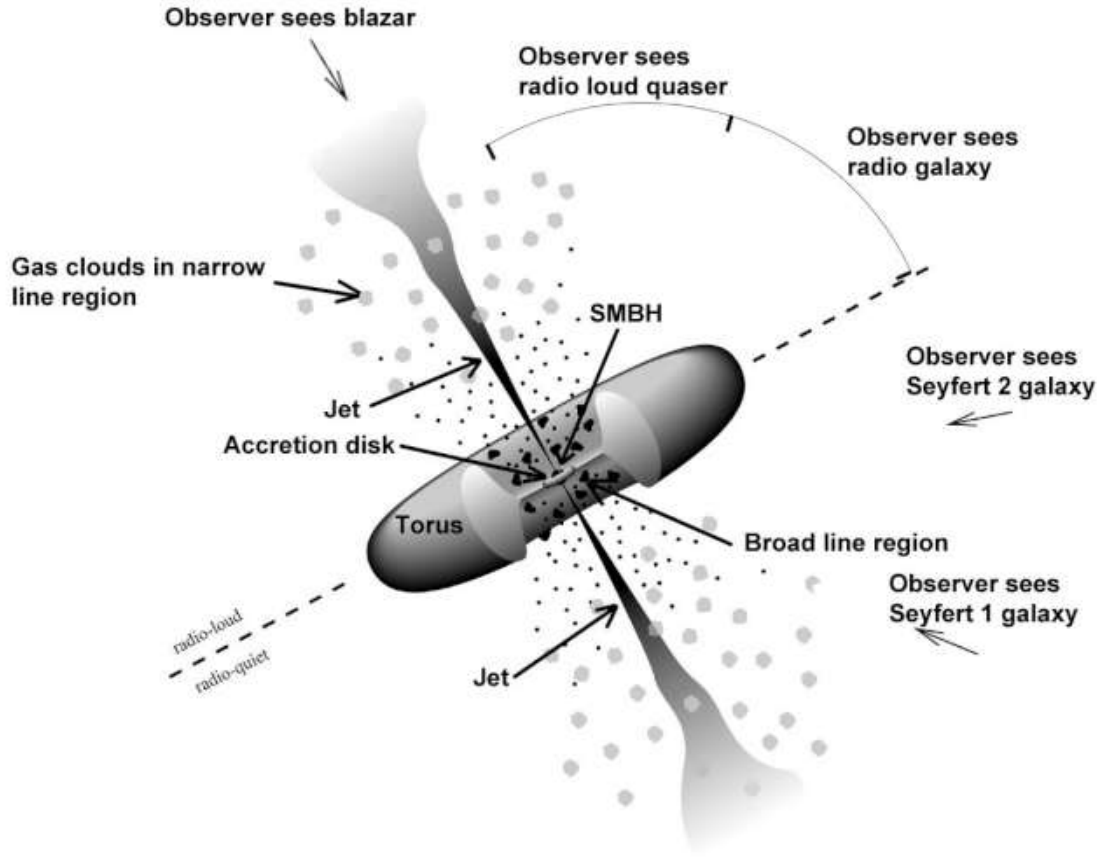


Figure 2.3: Unification model of an AGN (Fermi Gamma-ray Space Telescope 2025).

### 2.1.4 Variability

Apart from changing-look AGNs, which change their observed type over time, many AGNs like NGC 4593 show continuous and significant variability in their emission. This variability is observed across the electromagnetic spectrum and spans timescales from hours to several years, making it a key characteristic of active galaxies. Higher-energy emission, such as X-rays, typically shows faster and stronger fluctuations than optical or infrared radiation, with variability amplitudes and timescales generally decreasing towards lower photon energies. Those changing timescales can be spanning from hours, to day, to years and are generally random (Ulrich, Maraschi, and C. M. Urry 1997).

This variability is linked to instabilities within the accretion flow around the supermassive black hole. Processes such as magnetic turbulence in the corona, local fluctuations in the accretion rate, and thermal inhomogeneities within the disk are thought to drive the observed flux changes. While short-term variations are likely related to processes in the inner corona and disk, slower changes originate from propagating fluctuations in the outer regions that modulate emission at larger radii.

(Hagen et al. 2024).

This intrinsic variability plays a central role in reverberation mapping which will be talked about in the next section.

## 2.2 Reverberation Mapping

The main focus of this work is a classic reverberation mapping analysis of the Broad Lines of NGC 4593. This observational technique allows to probe the structure of the BLR around the SMBH inside the AGN. This technique bases on the time delay or time lag between the continuum's variation and the correlated response of the broad lines. With this calculable time lag it is possible to assume the geometry of the BLR and calculating the mass of the SMBH.

### 2.2.1 Principle

The fundamental assumption in reverberation mapping is that fluctuations in the observed continuum luminosity drive corresponding fluctuations in the emission-line flux, with a time delay. Like mentioned earlier, continuum fluctuations from the accretion disk serve as the ionizing source, illuminating the surrounding BLR. With variation in the continuum luminosity, the emission-line response follows these continuum variations with a measurable time lag (E. M. Cackett, M. C. Bentz, and Kara 2021). This time lag  $\tau$  is corresponding to the average light-travel distance from the photoionization continuum to the line emitting regions. Furthermore it is possible to approximate the characteristic radius of the BLR depending on  $\tau$  following this approximation:  $R_{\text{BLR}} \approx c \cdot \tau$ . With different time lags from emission lines origination from different regions it is possible to infer the geometry of the BLR. A BLR with a thin shell of clouds would produce a more uniform lag, whereas a broad distribution of clouds produces a range of lags. In principle, reverberation mapping can be used to 'map' the BLR's structure by inverting the delays (Bradley M. Peterson 1997). The response of the BLR's lines is typically assumed as linearly related tho the photo-ionization continuum, leading to the convolution expression:

$$L(t) = \int \Psi(\tau) C(t - \tau) d\tau \quad (2.1)$$

where  $\Psi(\tau)$  is the transfer function, delivering the BLR's geometric and kinematic information (Horne et al. 2004). While in theory the response of the BLR can be fully described by the transfer function  $\Psi(\tau)$ , this thesis focuses on measuring the

time lag between continuum and line variations. This lag can be estimated using cross-correlation techniques, which are discussed in the following section.

### 2.2.2 Cross-Correlation Function and Lag Measurement

In practice, recovering the full transfer function  $\Psi(\tau)$  would require very well-sampled and high signal-to-noise light curves over a duration much longer than the expected lag. Since real monitoring campaigns are often affected by observational gaps and noise, such reconstructions are rarely possible (Horne et al. 2004; B. M. Peterson 1993). For this reason, this thesis concentrates on measuring the mean time lag between continuum and emission-line variations using the Interpolated Cross-Correlation Function (ICCF) method.

Measuring the same objects over a span of time, it is possible to determine the correlation coefficient (CCF) as a function of the time shift  $\tau$  between two light curves, e.g. the variable light curve of the ionizing continuum and the light curve of a broad emission line. By sliding one curve relative to the other, the ICCF quantifies how well the variations match for each lag. In this context, two types of lags are defined: the lag corresponding to the maximum correlation  $\tau_{\text{peak}}$  and the centroid lag  $\tau_{\text{centroid}}$ .  $\tau_{\text{centroid}}$  gets calculated over all points of the CCF, that are above a selected threshold which is typically 80% of the CCF. Since the centroid lag is generally considered a more robust representation of the mean light-travel time of the BLR (B. M. Peterson, Ferrarese, et al. 2004), it is used in this thesis.

The uncertainty of the measured lag is estimated using a Monte Carlo approach combining Flux Randomization (FR) and Random Subset Selection (RSS) (B. M. Peterson, Wanders, et al. 1998; B. M. Peterson, Ferrarese, et al. 2004). In the FR step, each flux value is randomly perturbed according to its measurement uncertainty. In the RSS step, a subset of the data points is drawn at random with replacement, preserving the original sample size. For each realization, the ICCF analysis is repeated, resulting in a distribution of centroid lags. The median of this distribution is adopted as the final lag measurement, while the 16th and 84th percentiles are taken as the  $1\sigma$  confidence interval, accounting for both measurement noise and the effects of uneven temporal sampling.

### 2.2.3 Black-Hole Mass

With the measured rest-frame centroid lag  $\tau_{\text{centroid}}$  from the ICCF analysis and the velocity width of the broad emission line, the mass of the central supermassive black hole (SMBH) can be estimated under the assumption that the BLR gas is



gravitationally bound and its motions are dominated by the SMBH potential (B. M. Peterson, Ferrarese, et al. 2004). The distance to the BLR is given by

$$R_{\text{BLR}} = c \cdot \tau_{\text{centroid}} \quad (2.2)$$

and, combined with the line-of-sight velocity dispersion  $\Delta V$  of the BLR gas, the virial product is defined as

$$M_{\text{vir}} = \frac{R_{\text{BLR}} \Delta V^2}{G}. \quad (2.3)$$

The physical black hole mass is then obtained by applying a scale factor  $f$ , which accounts for the unknown geometry, kinematics, and inclination of the BLR:

$$M_{\text{BH}} = f \cdot M_{\text{vir}}. \quad (2.4)$$

Following Onken et al. (2004), a mean value of  $f$  is adopted, calibrated by aligning reverberation-based masses with the  $M_{\text{BH}} - \sigma_*$  relation observed in quiescent galaxies.

## 2.3 Bowen Fluorescence

The mechanism known as Bowen Fluorescence was first described by I.S. Bowen in 1934 to explain unexpected emission lines in nebular spectra (Bowen 1934). It is a multi-stage process called resonant line pumping, where photons emitted by an ion are absorbed by a different kind of ion due to a near-wavelength coincidence. This leads to enhanced emission lines that would otherwise be too weak to detect through normal recombination or collisional excitation. In AGN, Bowen Fluorescence typically involves HeII Lyman- $\alpha$  photons at 303.78Å, which excite OIII ions and, in a secondary step, NIII ions. The result is the emission of characteristic ultraviolet and optical lines (Selvelli et al. 2007; Baldini, Rossi, Arcodia, et al. 2023).

Similar fluorescence processes are also known for other ions. In this work, particular focus is placed on the OI $\lambda$ 8446 emission line. Its strength cannot be explained by recombination processes alone and is commonly attributed to Ly $\beta$  fluorescence. In this process, hydrogen Ly $\beta$  photons at 1025.72Å are absorbed by neutral oxygen due to a near-resonant transition. This enhances the OI emission through a separate, but related, fluorescence mechanism (Grandi 1980).

Although Ly $\beta$ -pumped OI $\lambda$ 8446 emission is independent of the classical Bowen mechanism, both processes share the fundamental principle of resonant line pumping, where photons from one species excite another species. As a result, both mech-

anisms provide valuable diagnostic information about the physical conditions and radiation field in AGN broad-line regions (Grandi 1980; Selvelli et al. 2007). In this work, the  $\text{O I } \lambda 8446$  emission line is investigated in the context of possible fluorescence excitation in NGC 4593.

## 3. Campaign and Analysis

The Analysis of this campaign bases of the observation campaign of NGC4593 in 2016 by Edward M. Cackett (Edward M Cackett et al. 2018). The observations took place between the 12th of July and the 6th of August with 26 successful observations out of 27 and was performed with the Hubble Space Telescope (HST) using the Space Telescope Imaging Spectrograph (STIS). The following section will cover important properties of NGC4593 and the 2016 campaign.

### 3.1 NGC4593

NGC 4593 is an active galactic nucleus (AGN), classified as a Seyfert 1 galaxy with a (R)SB(rs)b barred spiral morphology. It is located in the southern sky at RA = 12:39:39.44, DEC =  $-05^{\circ}20'39.03''$  (J2000) and has a redshift of  $z = 0.0083 \pm 0.0005$ , corresponding to a distance of about 35.6 Mpc (SIMBAD 2025) based on the  $\Lambda$ CDM model. The galaxy exhibits a prominent large-scale bar and nuclear dust ring connected to dust lanes along the bar, which likely channel gas toward the central region (Mulchaey and Regan 1997), as seen in figure 3.1. The AGN shows strong broad emission lines in H $\alpha$ , H $\beta$ , H $\gamma$ , Ly $\alpha$ , He I, and He II (Misty C Bentz and Katz 2015), indicating a well-developed broad-line region. Reverberation mapping of the broad H $\beta$  line yields a supermassive black hole mass of  $M = (7.63 \pm 1.62) \times 10^6 M_{\odot}$  (Misty C Bentz and Katz 2015), with a corresponding broad-line region radius of only a few light-days (Denney et al. 2006). Multi-wavelength monitoring has revealed strong variability from X-ray to optical bands, with interband time delays indicating a UV/optical-emitting accretion disk about three times larger than predicted by standard thin-disk theory and signatures of diffuse continuum emission from the BLR, particularly around the Balmer jump (Edward M Cackett et al. 2018). ALMA observations further reveal a central molecular gas reservoir of  $\sim 10^8 M_{\odot}$  arranged in a one-armed spiral and a circumnuclear ring, as well as evidence for a mild molecular outflow on scales of a few hundred parsecs (García-Burillo et al. 2019), highlighting the interplay between bar-driven inflow and AGN feedback in this galaxy.

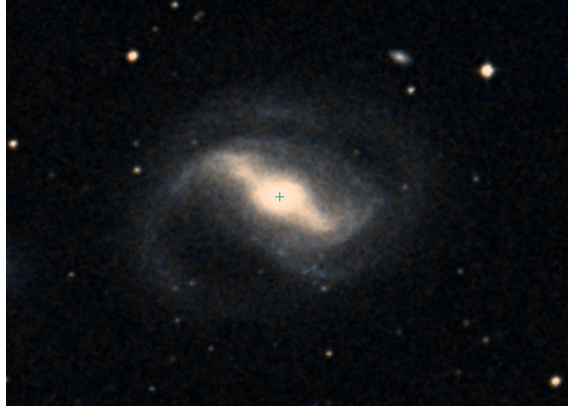


Figure 3.1: A DSS image of NGC4593.

## 3.2 2016 Campaign by E. M. Cackett

E. M. Cackett’s campaign was designed to study wavelength dependent continuum lags. Therefore, the STIS instrument on the Hubble Space Telescope was used with low-resolution gratings to measure a broad range of wavelengths. In each observation, spectra were taken using three different gratings: G140L, G430L, and G750L. These were used together with the  $52'' \times 0.2''$  slit.

The characteristics of the STIS gratings used in this analysis are summarized in Table 3.1. After a standard pipeline-processing, a package was used to do a Charge Transfer Inefficiency correction with an algorithm based on (Anderson and Bedin 2010). The few left rest of hot pixels got manually removed by interpolating the flux of neighbor pixels.

Table 3.1: Overview of STIS Grating Characteristics (Space Telescope Science Institute 2025)

Grating	Range [Å]	Exp. Time [s]	Res. Power	Dispersion [Å/pixel]
G140L	1119–1715	1234	$\sim 1000$	0.6
G430L	2888–5697	298	$\sim 500 - 1000$	2.73
G750L	5245–10233	288	$\sim 500 - 1000$	4.92

### 3.3 Intercalibration and Determination of AVG and RMS Spectra

Reverberation mapping requires multiple epochs to capture variability. For the 2016 campaign of NGC 4593, we retrieved 27 spectra from the ... archive of which 26 are usable for further analysis. The top panel of Figure 3.2 shows a section between about 4000 Å and 9000 Å of the optical spectral range from these epochs.

For the subsequent analysis, the average spectrum (AVG) is obtained by averaging over all epochs. Ideally, this improves the signal-to-noise ratio (S/N) sufficiently to identify spectral features in NGC 4593. Furthermore it is essential for the reverberation mapping analysis to identify variability between the epochs, which can be obtained with the root-mean-square (RMS) spectrum, defined as the standard deviation of the flux at each wavelength across epochs:

$$F_{\text{RMS}}(\lambda) = \sqrt{\frac{1}{N-1} \sum_{i=1}^N [F_i(\lambda) - \bar{F}(\lambda)]^2}, \quad (3.1)$$

with the mean spectrum at wavelength  $\lambda$  given by

$$\bar{F}(\lambda) = \frac{1}{N} \sum_{i=1}^N F_i(\lambda). \quad (3.2)$$

Constant features, like narrow emission lines, vanishes in the RMS spectrum, whereas variable components, like broad emission lines stands out. The top panel of Figure 3.3 shows the AVG and RMS spectra from the original retrieved data. It shows, that residual variability remains in nominally non-varying lines, especially in the forbidden features near 5000 Å. This indicates small wavelength misalignment between epochs. Therefore an intercalibration anchored to the narrow [O III]  $\lambda 5007$  line was performed. The lower panels of Figures 3.2 and 3.3 present the intercalibrated epochs and the corresponding AVG and RMS spectra. The disappearance of narrow features in the calibrated RMS spectrum confirms that the apparent variability in the uncalibrated RMS was induced by the wavelength shifts between the epochs rather than intrinsic line variability. For the most part, the intercalibrated AVG and RMS spectra are used in the following analysis. The exception will be for the measurement of the emission lines in the UV part of spectrum and their analysis. During the analysis of the UV emission lines it showed, that the results of the uncalibrated spectrum showed higher correlation then the results of the intercalibrated spectrum, which will be explained further in Chapter 4.

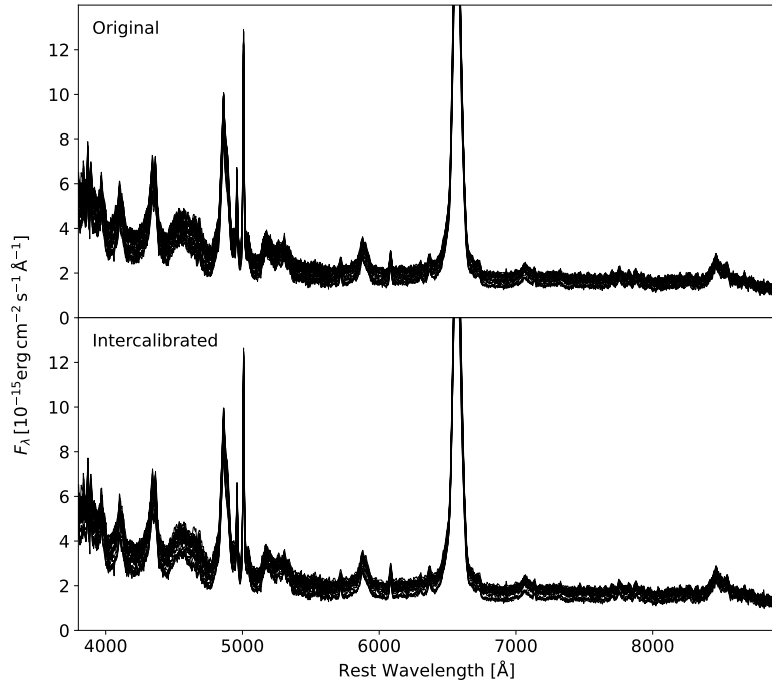


Figure 3.2: Comparison of the optical spectral range of the original spectra and the [O III]  $\lambda 5007$  intercalibrated spectra from the 2016 campaign of NGC 4593.

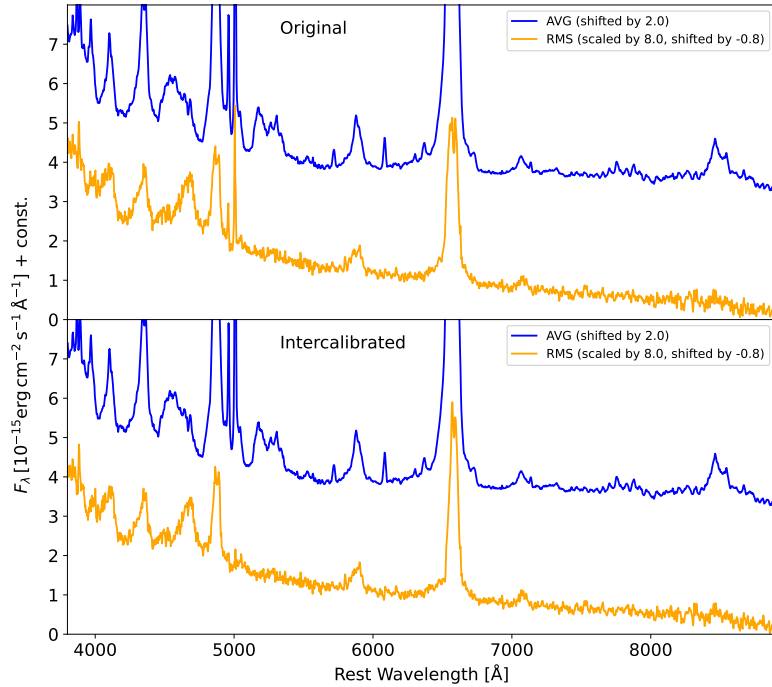


Figure 3.3: Comparison of the optical spectral range of the avg and rms spectra from the original data and the [O III]  $\lambda 5007$  intercalibrated data from the 2016 campaign of NGC 4593.

# 4. Reverberation Mapping Analysis of NGC4593

## 4.1 Line Determination

The AVG spectrum shows narrow emission lines, as well as broad emission lines, which is expected due to the Seyfert 1 classification of NGC4593. The first part of the reverberation mapping analysis is now the determination of Lines in the optical part of the spectrum (4.1) and the UV part between 1100 and 1700 Å (4.2).

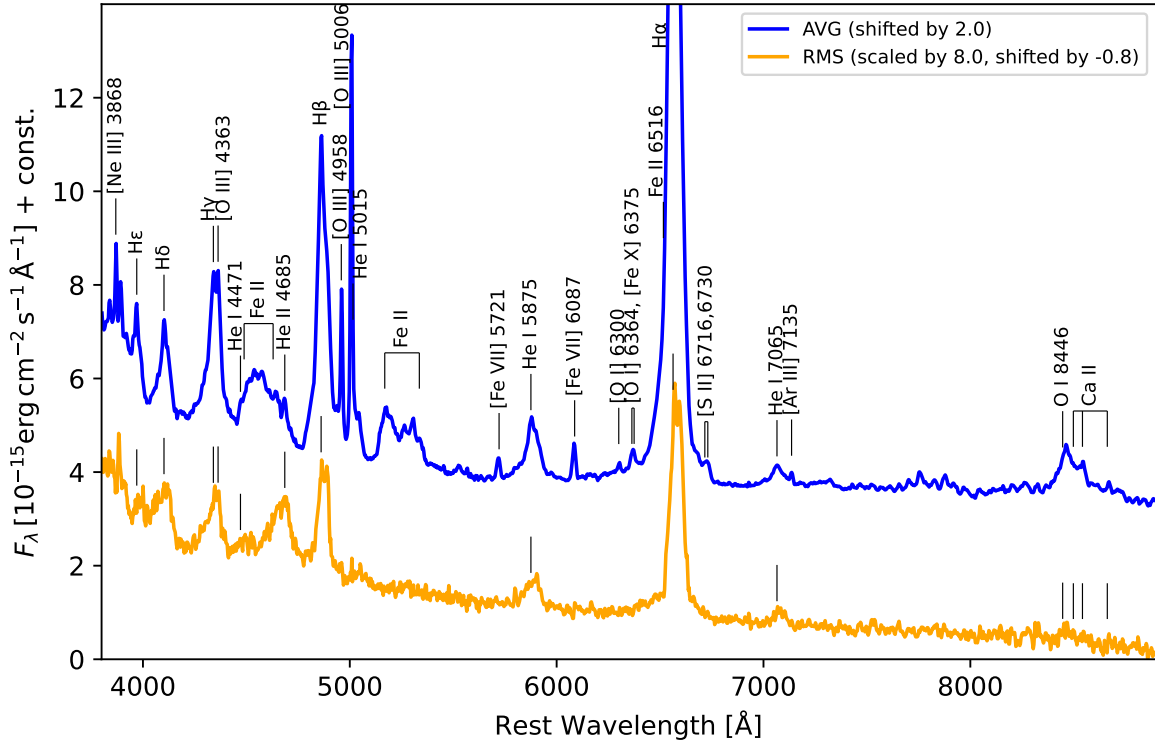


Figure 4.1: AVG RMS spectrum

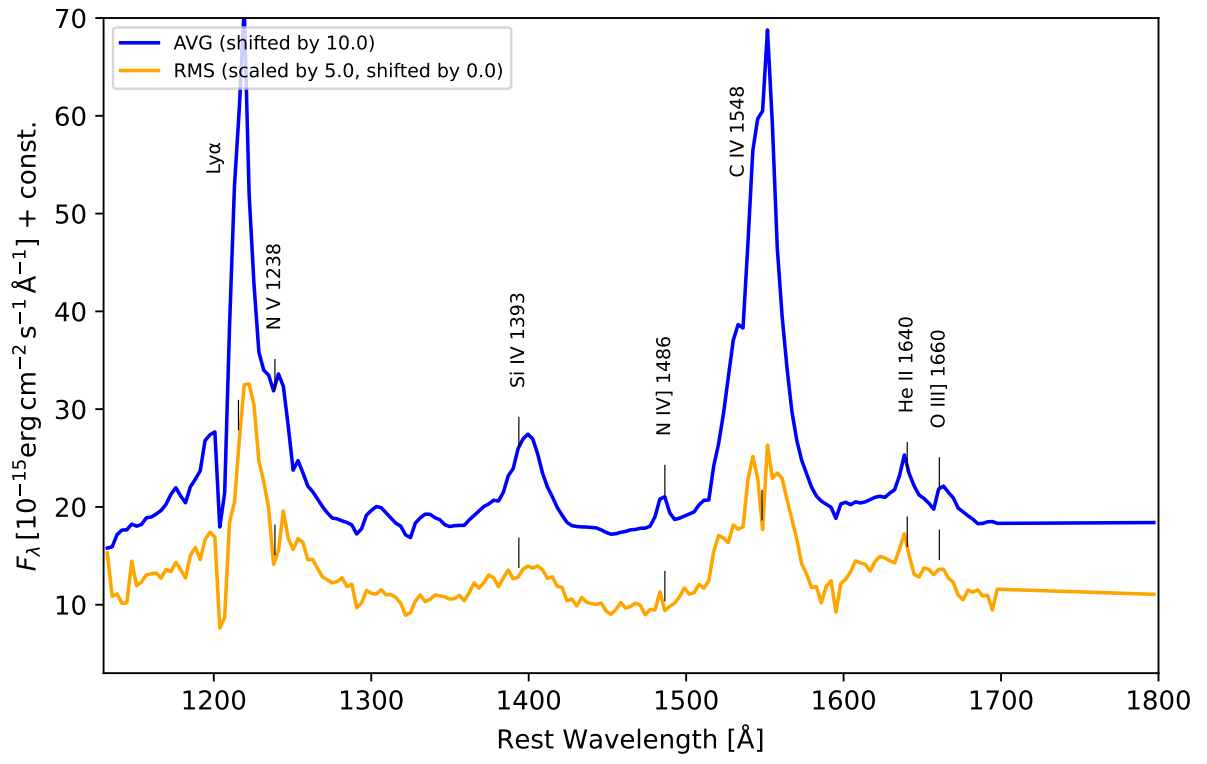


Figure 4.2: AVG RMS spectrum



## **4.2 Lightcurves**

...

### **4.2.1 Continua**

...

### **4.2.2 Emission Lines**

...

## **4.3 Line Profiles**

## **4.4 Time Lag and BH Masses**

## **4.5 Bowen Fluorescence**

# NGC4593 Continua

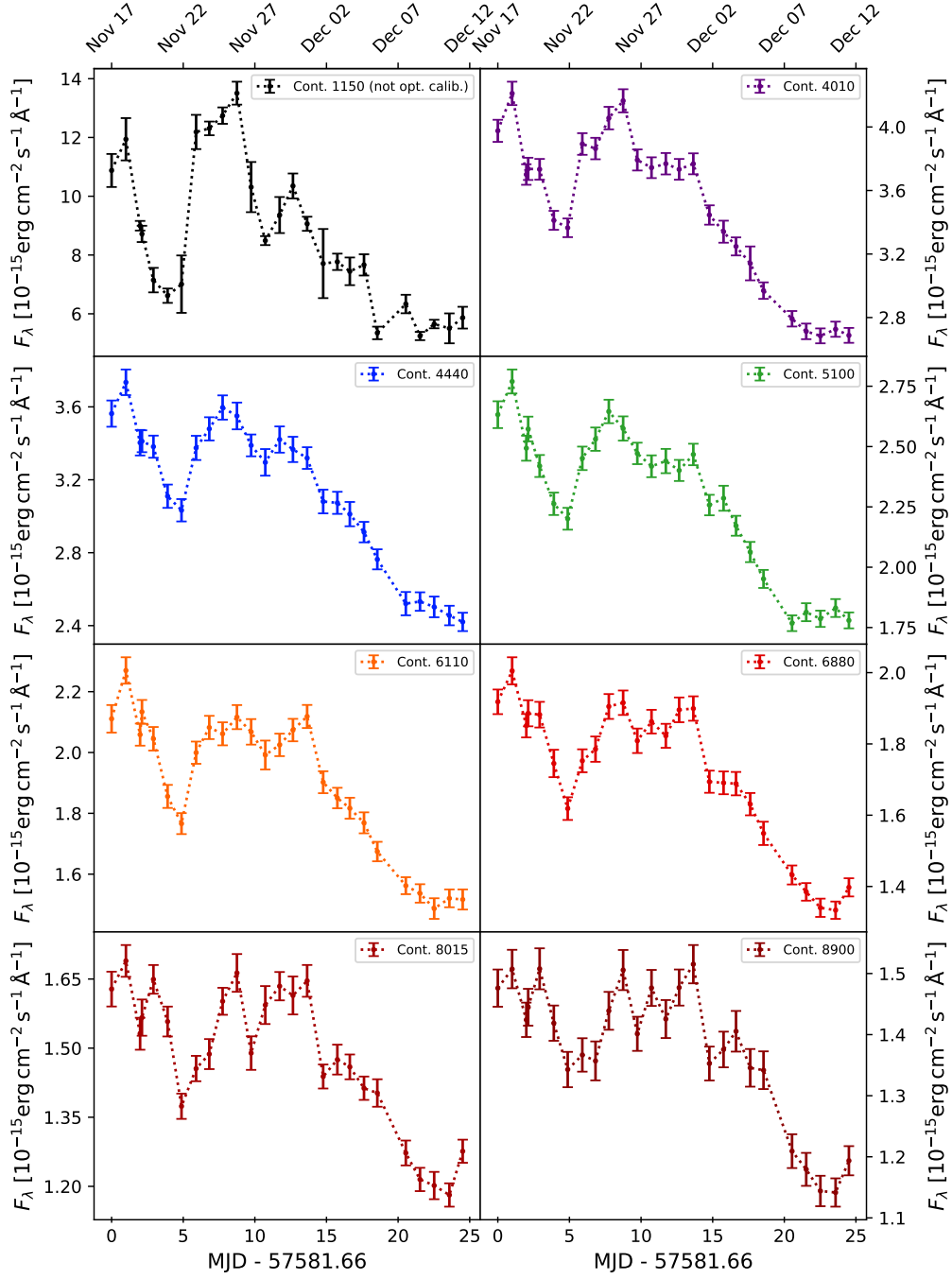


Figure 4.3: AVG RMS Spektrum

# NGC4593 Lines

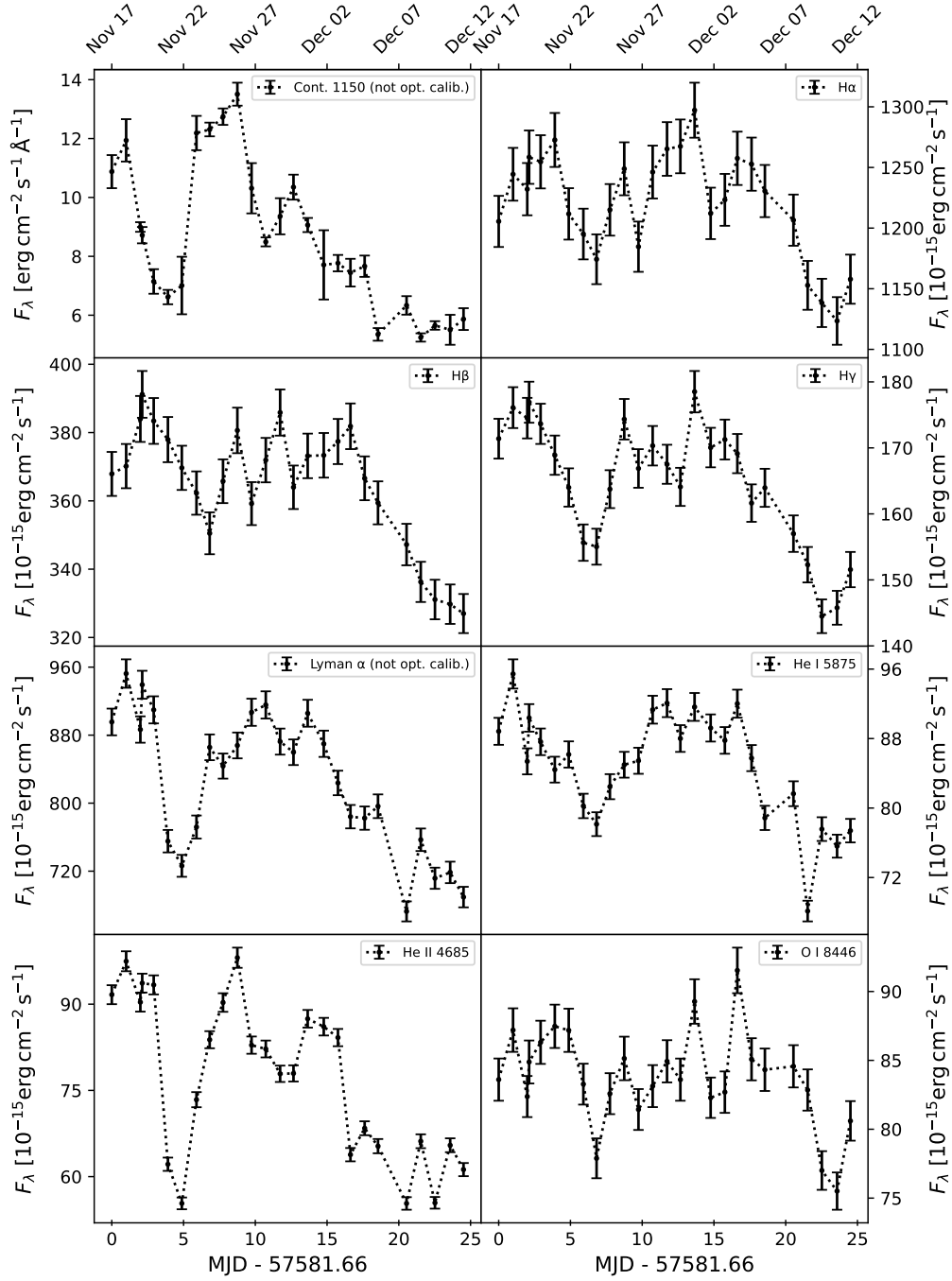


Figure 4.4: AVG RMS Spektrum

# Normalized Line Profiles

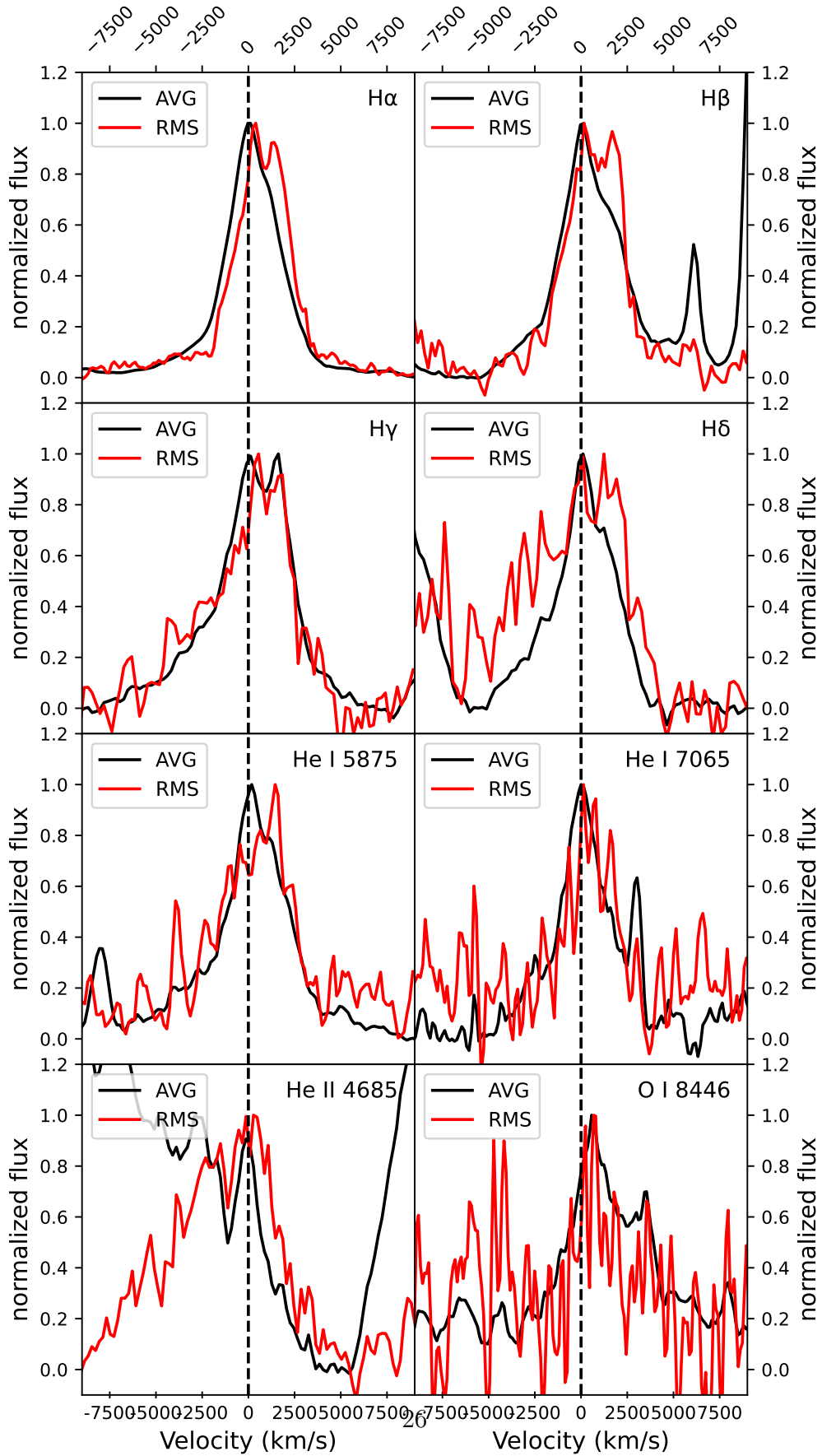


Figure 4.5: AVG RMS Spektrum

# CCFs between Emission Lines and UVW2 for NGC4593

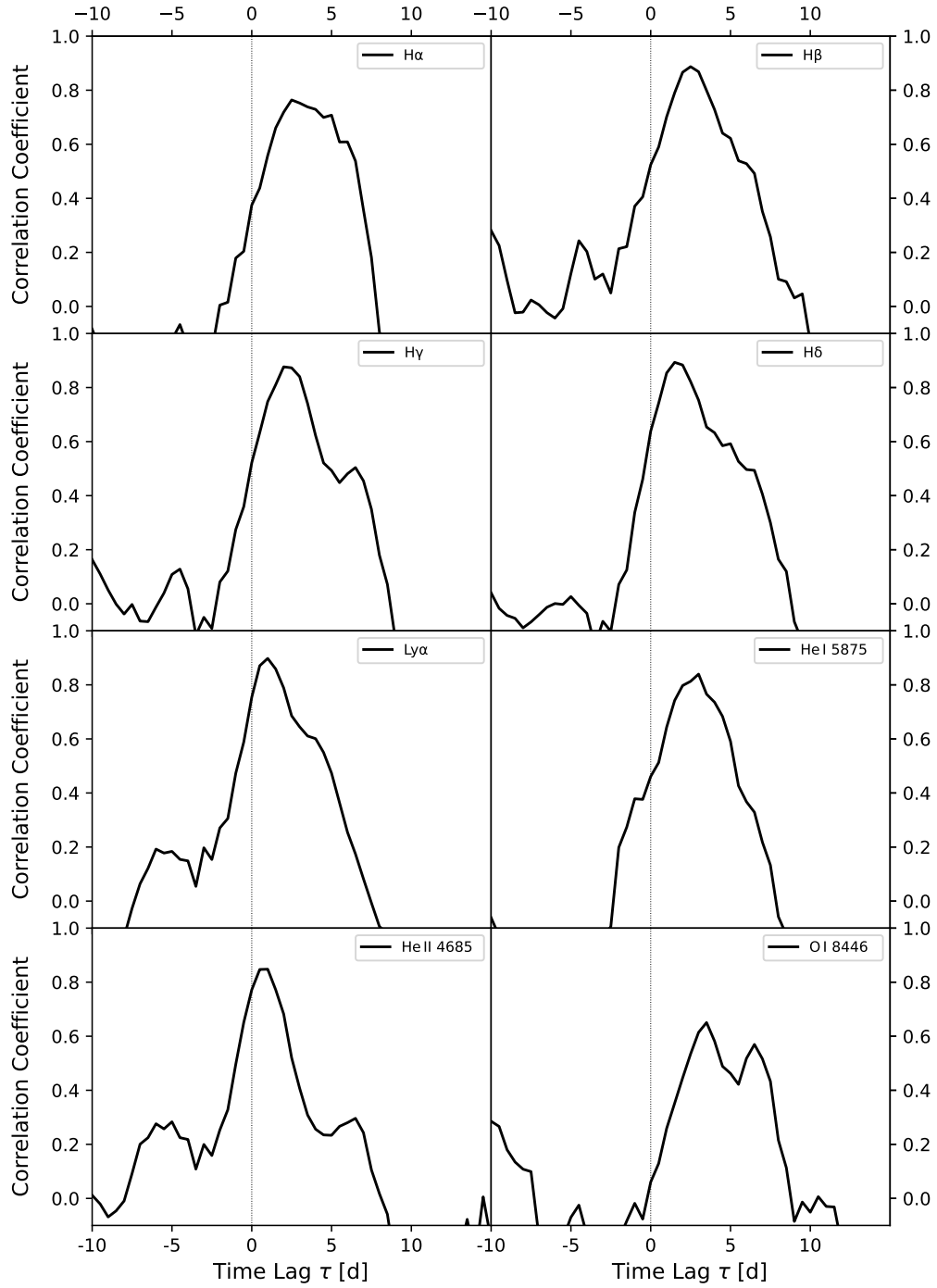


Figure 4.6: AVG RMS Spektrum

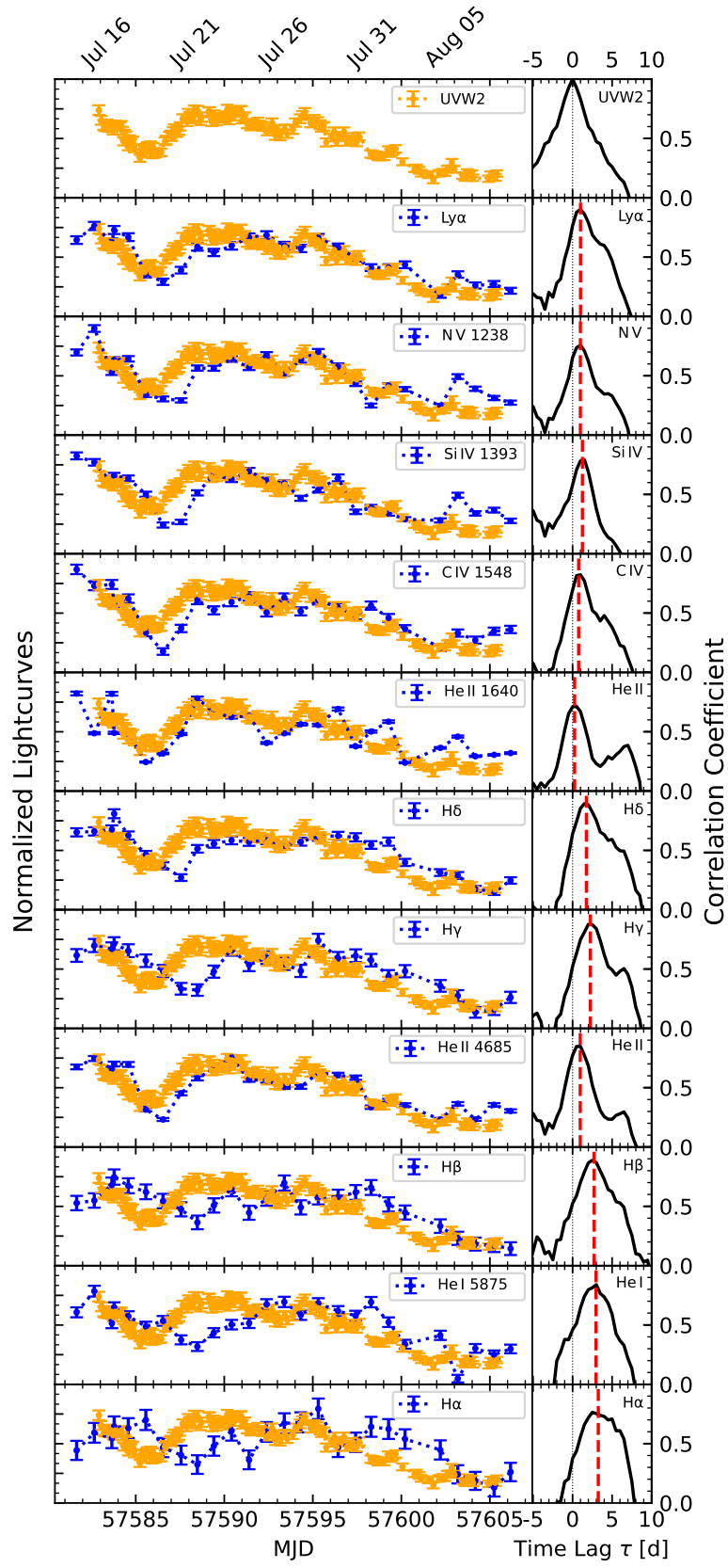


Figure 4.7: AVG RMS Spektrum

## 5. Discussion

# Bibliography

- Anderson, Jay and Luigi R Bedin (2010). “An empirical pixel-based correction for imperfect cte. i. hst’s advanced camera for surveys1”. In: *Publications of the Astronomical Society of the Pacific* 122.895, p. 1035.
- Antonucci, Robert (1993). “Unified models for active galactic nuclei and quasars”. In: *Annual Review of Astronomy and Astrophysics* 31, pp. 473–521. DOI: 10.1146/annurev.aa.31.090193.002353.
- Baldini, P., E. M. Rossi, R. Arcodia, et al. (2023). “A Bowen fluorescence flare as evidence of line pumping in a transient event”. In: *arXiv e-prints*. arXiv:2507.05342. arXiv: 2507.05342.
- Bentz, Misty C and Sarah Katz (2015). “The AGN black hole mass database”. In: *Publications of the Astronomical Society of the Pacific* 127.947, p. 67.
- Bowen, I. S. (1934). “The Excitation of the Nebulium Spectrum”. In: *Publications of the Astronomical Society of the Pacific* 46, pp. 146–149. DOI: 10.1086/124349.
- Cackett, E. M., M. C. Bentz, and E. Kara (2021). “Reverberation Mapping of Active Galactic Nuclei: From X-ray Corona to Dusty Torus”. In: *iScience* 24.12, p. 102557. DOI: 10.1016/j.isci.2021.102557.
- Cackett, Edward M et al. (2018). “Accretion disk reverberation with Hubble space telescope observations of NGC 4593: evidence for diffuse continuum lags”. In: *The Astrophysical Journal* 857.1, p. 53.
- Denney, Kelly D. et al. (Dec. 2006). “The mass of the black hole in the Seyfert 1 galaxy NGC 4593 from reverberation mapping”. In: *Astrophysical Journal Letters* 653, pp. 152–158. DOI: 10.1086/508533.
- Fermi Gamma-ray Space Telescope (2025). *Figure 1: Spectral Energy Distribution of an AGN*. URL: <https://fermi.gsfc.nasa.gov/science/etev/agn/figure1.jpg> (visited on 06/19/2025).
- García-Burillo, S. et al. (2019). “ALMA images the many faces of the NGC1068 torus and its surroundings”. In: *Astronomy & Astrophysics* 632, A61. DOI: 10.1051/0004-6361/201936606.



- Grandi, S. A. (May 1980). “OI lambda 8446 emission in Seyfert 1 galaxies.” In: 238, p. 10. DOI: 10.1086/157952.
- Hagen, L. M. Z. et al. (2024). “What Drives the Variability in AGN? Insights from Disk Reprocessing and Inhomogeneous Accretion”. In: *Monthly Notices of the Royal Astronomical Society* 530, pp. 4850–4874. DOI: 10.1093/mnras/stad3782.
- Hickox, Ryan C. and David M. Alexander (2018). “Obscured Active Galactic Nuclei”. In: *Annual Review of Astronomy and Astrophysics* 56, pp. 625–671. DOI: 10.1146/annurev-astro-081817-051719. arXiv: 1806.04680 [astro-ph.GA].
- Horne, Keith et al. (2004). “Observational Requirements for High-Fidelity Reverberation Mapping”. In: *Publications of the Astronomical Society of the Pacific* 116.819, p. 465.
- Mo, Houjun, Frank van den Bosch, and Simon White (2010). *Galaxy Formation and Evolution*. Cambridge University Press. ISBN: 9780521857932.
- Mulchaey, John S. and Michael W. Regan (June 1997). “The Fueling of Nuclear Activity: II. The Bar Properties of Seyfert and Normal Galaxies”. In: *The Astrophysical Journal Letters* 482.2, pp. L135–L138. DOI: 10.1086/310710.
- Netzer, Hagai (2013). *The Physics and Evolution of Active Galactic Nuclei*. Cambridge: Cambridge University Press.
- Onken, C. A. et al. (2004). “Supermassive Black Holes in Active Galactic Nuclei. II. Calibration of the Black Hole Mass-Velocity Dispersion Relationship for Active Galactic Nuclei”. In: *The Astrophysical Journal* 615, pp. 645–651. DOI: 10.1086/424655.
- Osterbrock, Donald E. (1989). *Astrophysics of Gaseous Nebulae and Active Galactic Nuclei*. Mill Valley, California: University Science Books. ISBN: 9780935702111.
- Osterbrock, Donald E. and Richard W. Pogge (1985). “The spectra of narrow-line Seyfert 1 galaxies”. In: *The Astrophysical Journal* 297, pp. 166–176. DOI: 10.1086/163513.
- Peterson, B. M. (1993). “Reverberation Mapping of Active Galactic Nuclei”. In: *Publications of the Astronomical Society of the Pacific* 105, pp. 247–268. DOI: 10.1086/133140.
- Peterson, B. M., L. Ferrarese, et al. (2004). “Central Masses and Broad-Line Region Sizes of Active Galactic Nuclei. II. A Homogeneous Analysis of a Large Reverberation-Mapping Database”. In: *The Astrophysical Journal* 613, pp. 682–699. DOI: 10.1086/423269.
- Peterson, B. M., I. Wanders, et al. (1998). “Optical Continuum and Emission-Line Variability of Seyfert 1 Galaxies”. In: *The Astrophysical Journal* 501, pp. 82–93. DOI: 10.1086/305813.

- Peterson, Bradley M. (1997). *An Introduction to Active Galactic Nuclei*. Cambridge University Press. ISBN: 9780521473484.
- ResearchGate (2025). *Frequency of Seyfert Type Transitions in a Sample of 102 Local Active Galactic Nuclei - Scientific Figure*. URL: [https://www.researchgate.net/figure/An-example-of-Seyfert-1-and-Seyfert-2-spectra-highlighting-their-differences-The-broad\\_fig1\\_304162356](https://www.researchgate.net/figure/An-example-of-Seyfert-1-and-Seyfert-2-spectra-highlighting-their-differences-The-broad_fig1_304162356) (visited on 09/08/2025).
- Ricci, Claudio et al. (2022). “Changing-look Active Galactic Nuclei”. In: *Nature Astronomy* 6, pp. 1342–1354. DOI: 10.1038/s41550-022-01796-7.
- Selvelli, P. et al. (2007). “The Bowen fluorescence lines in the spectrum of RR Telescopii”. In: *Astronomy and Astrophysics* 464, pp. 715–728. DOI: 10.1051/0004-6361:20066616.
- Seyfert, Carl K. (1943). “Nuclear Emission in Spiral Nebulae”. In: *The Astrophysical Journal* 97, pp. 28–40. DOI: 10.1086/144488.
- Shakura, N. I. and R. A. Sunyaev (1973). “Black holes in binary systems. Observational appearance”. In: *Astronomy and Astrophysics* 24, pp. 337–355.
- SIMBAD (2025). *NGC4593*. URL: <https://simbad.u-strasbg.fr/simbad/sim-id?Ident=NGC4593> (visited on 06/10/2025).
- Space Telescope Science Institute (2025). *STIS Instrument Handbook: Gratings*. URL: <https://hst-docs.stsci.edu/stisihb/chapter-13-spectroscopic-reference-material/13-3-gratings> (visited on 05/12/2025).
- Ulrich, M.-H., L. Maraschi, and C. M. Urry (1997). “Variability of Active Galactic Nuclei”. In: *Annual Review of Astronomy and Astrophysics* 35, pp. 445–502. DOI: 10.1146/annurev.astro.35.1.445.
- Urry, C. Megan and Paolo Padovani (1995). “Unified Schemes for Radio-Loud Active Galactic Nuclei”. In: *Publications of the Astronomical Society of the Pacific* 107.715, pp. 803–845. DOI: 10.1086/133630.